A Computational Investigation of the Impact of Multiple Injection Strategies on Combustion Efficiency in Diesel–Natural Gas Dual-Fuel Low-Temperature Combustion Engines

Lorenzo Bartolucci[1]
University of Rome Tor Vergata,
Rome 00133, Italy
e-mail: lorenzo.bartolucci@uniroma2.it

Stefano Cordiner
University of Rome Tor Vergata,
Rome 00133, Italy
e-mail: cordiner@uniroma2.it

Vincenzo Mulone
University of Rome Tor Vergata,
Rome 00133, Italy
e-mail: mulone@uniroma2.it

Sundar R. Krishnan
The University of Alabama,
Tuscaloosa, AL 35487
e-mail: skrishnan@eng.ua.edu

Kalyan K. Srinivasan
The University of Alabama,
Tuscaloosa, AL 35487
e-mail: ksrinivasan@eng.ua.edu

Dual-fuel diesel–methane low-temperature combustion (LTC) has been investigated by various research groups, showing high potential for emissions reduction (especially oxides of nitrogen oxide (NO_x) and particulate matter (PM)) without adversely affecting fuel conversion efficiency in comparison with conventional diesel combustion. However, when operated at low load conditions, dual-fuel LTC typically exhibits poor combustion efficiencies. This behavior is mainly due to low bulk gas temperatures under lean conditions, resulting in unacceptably high carbon monoxide (CO) and unburned hydrocarbon (UHC) emissions. A feasible and rather innovative solution may be to split the pilot injection of liquid fuel into two injection pulses, with the second pilot injection supporting CO and UHC oxidation once combustion is initiated by the first one. In this study, diesel–methane dual-fuel LTC is investigated numerically in a single-cylinder heavy-duty engine operating at 5 bar brake mean effective pressure (BMEP) at 85% and 75% percentage of energy substitution (PES) by methane (taken as a natural gas (NG) surrogate). A multidimensional model is first validated in comparison with the experimental data obtained on the same single-cylinder engine for early single pilot diesel injection at 310 crank angle degrees (CAD) and 500 bar rail pressure. With the single pilot injection case as baseline, the effects of multiple pilot injections and different rail pressures on combustion and emissions are investigated, again showing good agreement with the experimental data. Apparent heat release rate and cylinder pressure histories as well as combustion efficiency trends are correctly captured by the numerical model. Results prove that higher rail pressures yield reductions of HC and CO by 90% and 75%, respectively, at the expense of NO_x emissions, which increase by ~30% from baseline still remaining at very low level (under 1 g/kWh). Furthermore, it is shown that postinjection during the expansion stroke does not support the stable development of the combustion front as the combustion process is confined close to the diesel spray core. [DOI: 10.1115/1.4047887]

Keywords: engine efficiency, low temperature combustion, dual-fuel combustion, natural gas technology

Introduction

Rational evaluation of international energy security must include a critical re-examination of the approaches for achieving high efficiency clean combustion using alternative fuels. The Basic Energy Sciences Workshop on Basic Research Needs for Clean and Efficient Combustion of 21st Century Transportation Fuels of the US Department of Energy in 2009 identified that the monolithic nature of transportation technologies offers the greatest opportunity to realize efficiency improvements of up to 25–50% [1]. While light-duty passenger cars and pickup trucks are moving toward increasing levels of hybridization/electrification, commercial freight transport trucks, which accounted for 23% of transportation energy demand in 2017 [2], still mostly employ heavy-duty diesel engines (HDDEs) with a substantially lower appetite for hybridization/electrification. This is because the bottom line for truck fleets is the cost per ton-mile of freight that can be reliably transported, and therefore, the additional space and weight requirements for hybridization/electrification (e.g., batteries and motors) adversely affect this bottom line. Consequently, there is an imperative need to improve the fuel conversion efficiencies (FCEs), pollutant exhaust emissions (primarily, nitrogen oxide—NO_x—and particulate matter (PM)), and greenhouse gas (GHG) emissions from HDDEs, particularly, with the upcoming phase 2 GHG reductions from HD truck engines that call for a 6% CO_2 reduction from the 2017 levels [3] and additional stringent engine-out NO_x levels [4]. The U.S. Department of Energy SuperTruck I program that demonstrated 50% brake thermal efficiency (BTE) in HDDE for transportation and the follow-up SuperTruck II program that aims to achieve 55% BTE in next-generation HD trucks bear testimony to the extensive research that has happened over the last 10 years to simultaneously improve HDDE efficiency and to reduce emissions [5].

Recent developments in advanced combustion concepts have focused on using two fuels of different propensities to autoignition to achieve high FCEs and ultra low NO_x emissions [6–8]. These combustion concepts introduce a low reactivity fuel (e.g., natural

[1]Corresponding author.

Contributed by the Internal Combustion Engine Division of ASME for publication in the Journal of Energy Resources Technology. Manuscript received May 20, 2020; final manuscript received June 30, 2020; published online August 27, 2020. Assoc. Editor: Samer F. Ahmed.

gas or gasoline) through the intake manifold to create a premixed charge, which is compression-ignited using a high-pressure, high reactivity fuel spray (e.g., diesel) [9,10]. These dual-fuel low-temperature combustion (LTC) concepts, using natural gas, have immense potential to reduce CO_2 emissions; however, there is the added risk of "methane slip," i.e., any amount of unburned natural gas that escapes the tailpipe posing a risk. For example, if the engine-out methane emissions are greater than 0.1 g/bhp h, then they must be multiplied by a global warming potential factor of 34 [7]. A particular scenario of concern occurs at low engine loads where the coauthors and other researchers have observed instances of high engine-out unburned hydrocarbon (UHC) and carbon monoxide (CO) emissions and high cyclic combustion variations [10–12]. Our previous studies [13–17] on diesel–natural gas (NG) and diesel–methane dual-fuel LTC, as well as those of other research groups (e.g., Refs. [18–20]), have clearly established that very low engine-out NO_x (<0.2 g/kWh) and PM (<0.1 filter smoke number) emissions can be achieved with careful control of pilot fuel injection timing (SOI), pilot fuel injection pressure, and intake boost pressure over a range of engine loads (brake mean effective pressure (BMEP) from 2.5 to >10 bar). To reduce UHC and CO emissions at low engine loads, we have investigated hot (uncooled) exhaust gas recirculation (EGR) in previous studies [16,18,19] and demonstrated reductions of up to 70% in UHC and 40% in CO at low loads. Königsson et al. [20] studied the impact of crevice volumes on engine-out UHC emissions from dual-fuel engines. Their major conclusion is that if the combustion phasing favors more complete UHC oxidation, e.g., at high diesel energy fractions, the predominant source of UHC emissions in dual-fuel engines may be attributed to crevice hydrocarbons, particularly from the topland crevices. In particular, they note that the main reason for such high UHC emissions from the crevices is likely due to poor oxidation rates of the hydrocarbons that migrate out of the crevices into the combustion chamber later in the expansion stroke when the bulk gas temperatures are lower. As a consequence, they propose the employment of additional diesel injections later in the expansion stroke to increase the bulk gas temperture and to reduce cyclic combustion variations. These findings, particularly that of using multiple diesel injections, e.g., late postinjections, to reduce engine-out hydrocarbons, were well supported by preliminary experiments conducted by our research group [21]. These experiments explored the impact of dual pilot injections on diesel–methane dual-fuel LTC in a 1.827 L medium-duty single-cylinder research engine (SCRE) at low engine loads. Even with unoptimized operation, our dual-diesel pilot injection experiments showed significant reductions in UHC and CO emissions along with higher indicated fuel conversion efficency, albeit with some NO_x penalties. This article is a numerical computational fluid dynamics (CFD) investigation to determine the cause–effect relations that further corroborate the late postinjection hypothesis made by Königsson et al. [20] and experimental observations made by Sohail [21]. The specific objectives of this work include:

- investigation of the influence of the spray–charge motion interaction on the ignition and combustion processes, particularly, to capture the impact of the late post-injection on local charge motion and mixing,
- investigation of the influence of the rail pressure on the combustion process,
- investigation of the impact of the relative (crank angle) separation between the first pilot injection and the subsequent late injection, and
- investigation of the evolution of the combustion process, and unearth cause–effect relationships that might be useful in identifying strategies to further mitigate UHC emissions and simultaneously improve FCEs in dual-fuel LTC engines.

Experimental Setup

The experimental data used for CFD model validation in the present work were obtained by Krishnan, Srinivasan, and coworkers [21] on an SCRE. A 250 HP AC regenerative dynamometer (Dyne Systems), controlled by Interlock V engine controller coupled to the SCRE, was used to measure torque and speed. An integrated emissions bench (Altech Environment S.A.) was used to measure engine-out UHC, NO_x, CO, CO_2, and O_2 emissions. Additional information regarding the experimental setup is provided by Raihan [22].

Methane was fumigated into the intake manifold, allowing the formation of a premixed methane–air charge, which is burned by the ignition of one or more pilot injections of diesel fuel. A common rail system with the BOSCH injector (instrumented with a needle lift sensor) was used to provide the correct amount of diesel fuel. An external air compressor was used to provide compressed air for the SCRE, and intake and exhaust surge tanks helped minimize pulsations. The nominal compression ratio of the SCRE was 17.1:1. However, based on simulations performed to match the experimentally measured motoring pressure curves, the compression ratio was realized to be slightly lower. Table 1 presents the main parameters of the SCRE.

The experiments were conducted at steady-state, i.e., the engine was allowed to output constant BMEP and operate at constant percentage of energy substitution (PES), maintaining constant intake manifold pressure for 30 s before the start of data recording. The data points were selected in a calculated manner that result in a gradual decrease of UHC, NO_x, CO, and smoke emissions. The experiments were repeated three times, and standard error bars (68% confidence interval) indicate measurement variability. Additional information about the experimental procedure and results are provided by Sohail [21].

Three different operating points have been considered in the present work:

- *OP1:* A single-injection case with SOI at 310 crank angle degrees (CADs) with a rail pressure of 500 bar used as the baseline for performance and emissions comparison.
- *OP2:* Then, a second injection at 375 CAD is added to the first SOI at 310 CAD for the second operating condition.
- *OP3:* Finally, keeping the first SOI at 310 CAD and the second at 375 CAD for all subsequent data points, the benefits of increasing the rail pressure up to 1200 bar was studied.

For all the cases studied, the engine speed and load were fixed at 1500 rev/min and 5 bar BMEP, respectively, with a boost pressure of 1.5 bar. No EGR was employed for the tests.

Numerical Setup

The entire set of simulations was performed using CONVERGE, a CFD software suitable for internal combustion engine analysis [23]. Unlike many CFD programs, CONVERGE automatically generates a perfectly orthogonal, structured grid at runtime based on simple, user-defined grid control parameters. CONVERGE uses an innovative boundary-fitted approach eliminating the need for the computational grid to coincide with the geometry of interest. This method has two significant advantages. First, the type of grid used is chosen for computational efficiency instead of geometry.

Table 1 Engine parameters

Displacement volume	1.8275 l
Bore	142 mm
Stroke	128 mm
CR	17:1
Speed	1500 rpm
Injector	8 holes
Intake P and T	1.48 bar and 300 K
IVO–IVC	5–182 CAD
EVO–EVC	510–718 CAD

Note: CR: compression ratio; IVO: inlet valve opening; IVC: inlet valve closing; EVO: exhaust valve opening; and EVC: exhaust valve closing.

This process allows the use of simple orthogonal grids, which simplifies the numerics of the solver. Second, the grid generation complexity and the time required are greatly reduced, as the complex geometry only needs to be mapped onto the underlying orthogonal grid. In addition to its novel approaches to grid generation and boundary treatment, CONVERGE includes state-of-the-art numerical techniques and models for physical processes including turbulence, spray, combustion, conjugate heat transfer, and cavitation. With these models, CONVERGE can simulate a wide variety of flow problems. The models in CONVERGE have been extensively validated for internal combustion engine cases. Validation of the geometry and main simulation parameters has been presented in a previous article [24]. Temperature and pressure have been fixed at the inflow surface at 300 K and 1.48 bar, respectively. On the exhaust side, boundary conditions for pressure at the *outflow* were calculated iteratively to match the experimental intake gas mass flowrate (i.e., methane plus air flowrate). Fixed temperature boundary conditions were set for all the wall surfaces. Intake manifold surfaces were prescribed to have same temperature of intake air; the exhaust manifold was considered at 430 K liner, head, and piston temperatures were fixed at 410 K, 430 K, and 470 K, respectively. These values were set based on previous results on the same SCRE presented by Jha et al. [25]. Based on the previous studies on the dual-fuel combustion process [26,27], the diesel fuel initial temperature has been set at 450 K. Considering the spray itself, an essential input parameter is the rate of injection, which has been reconstructed using the tool developed by the CMT research group;[2] more details are provided in the following sections.

Spray discharge coefficient, breakup model constants, and spray cone angle are the main parameters affecting the spray behavior during the injection phase. Those constants have been carefully analyzed and calibrated in the previous works [24,28].

The Kelvin–Helmholtz spray breakup model with coupled aerodynamic effects (KH-ACT) has been used to obtain an accurate agreement in terms of penetration and entrainment characteristics [29]. The interaction between liquid droplet and solid surface has been modeled using drop/film splashing approach. This is based on O'Rourke's model that depends on the Weber number, the local film thickness, droplet diameters, and the local Reynolds number. Moreover a drop-drag dynamic model has been considered, taking into account the continuous variation of the droplet shape to estimate the penetration more accurately. Simulations have been carried out on an orthogonal Cartesian mesh with a base grid of 3 mm; two built-in strategies have been used to modify the grid in both space and time with embedding and adaptive mesh refinement (AMR). Spray-embedding of level 3 is activated immediately before the injection process onset and later deactivated after the end of the injection event. The AMR strategy foresees the generation of a finer mesh in given regions automatically activated by the software whenever a certain threshold for gradients of velocity, temperature, or specific chemical species is detected. In this article, an AMR of level 3 has been selected for each of these parameters inside the combustion chamber. This means that the dimension of a single computational cell can be decreased down to 0.375 mm. The overall number of cells ranged from a minimum about 300 k up to a maximum of almost 2.65 M. Simulations run on 36 cores Intel® Xeon® processor E5-2600 v4 at the CINECA facility.[3] The computational cost was about 2 days for a full cycle simulation requiring up to 128 GB of RAM. For each simulation, three cycles were performed to ensure that the results were independent of the initial conditions.

The entire series of simulations has been run with the Reynolds-averaged Navier–Stokes methodology and a renormalization group (RNG) k-ε turbulence model. The RNG approach [30] is based on two transport equations, the first related to the turbulent kinetic energy (k) and the second regarding the rate of dissipation of turbulent kinetic energy (ε). This model is rather standard for engine simulations with accurate modeling of turbulent transport effects.

CSU186 [31] is the selected multicomponent chemical kinetics mechanism based on 186 species and 1014 reactions developed specifically for diesel–NG dual-fuel engines. Since NG is mostly composed of methane, this mechanism may be expected to accurately capture the oxidation reactions of pure methane. A blend of n-dodecane and m-xylene with a mass percentage of 75% and 25%, respectively, has been used as diesel fuel surrogate [31]. It is worth highlighting that the same components have been simulated in both liquid and vapor phases, and all of the thermodynamic properties of these fuels are available in the CONVERGE Studio built-in fuel library. In particular, dependence with temperature has been taken into account for thermodynamic properties such as gas heat coefficients, density, vapor pressure, and surface tension. An example of the temperature dependence of surface tension for both n-dodecane and m-xylene is shown in Fig. 1 (left).

The inclusion of m-xylene allows consideing low-temperature reactions, providing an accurate representation of the low-temperature heat release (LTHR) observed experimentally and the onset of the subsequent propagation phase [31].

Special focus has been given to the validation of the chemical reaction mechanism to prove the robustness of the numerical results. Results for a 0-D constant volume ignition process have been compared with the experimental data collected for a high-pressure (50 bar and 150 bar) shock tube [34] at lean conditions. The experimental data were collected for a CH_4—air mixture corresponding to a global equivalence ratio of $\phi = 0.4$; the air composition for the numerical simulations were set according to the experimental data conditions in terms of oxygen and argon fractions. Figure 1 (right) shows a good correlation between the experimental and the numerical data over a wide temperature and pressure range. It is shown how the CSU 186 model behavior performs similarly to YAO [33] and POLIMI [32] models in accordance with the experimental data. At higher pressure, a better agreement is observed between the CSU 186 model and the experimental data compared to the other two models.

Results and Discussion

Results are presented in this section showing first the validation of the numerical data in comparison with the experimental data. Then, the effects of the double-injection process are demonstrated on the charge distribution and on the timing and behavior of the autoignition and combustion processes. Finally, pollutant emissions trends are analyzed.

Validation of the Numerical Model

Table 2 summarizes the main global parameters for the three simulated cases, showing a good agreement between experimental and numerical results in terms of trapped mass, PES, and combustion efficiency. To estimate the PES, the lower heating value for methane and diesel were set at 50 MJ/kg and 42.5 MJ/kg, respectively.

It is worth noting that, for both double-injection operating points, only the mean diesel flow rate was measured with an uncertainty on the diesel fuel mass split between the two injections. This ratio is, in fact, key for the obtainment of a good agreement between numerical and experimental results. The tool developed by the CMT research group[2] was used to estimate the diesel split based on injector current and rail pressure measurements. Two different spray rates were generated according to different duration and backpressure data, while the rail pressure was considered constant at 500 bar and 1200 bar for the OP2 and OP3 cases, respectively.

For OP2, 60% of the fuel is injected at 310 CAD, while the remaining fraction is injected at 375 CAD. The same procedure is used for the OP3 case, leading to a different diesel mass percentage

[2]https://www.cmt.upv.es/ecn03.aspx
[3]https://www.cineca.it/en

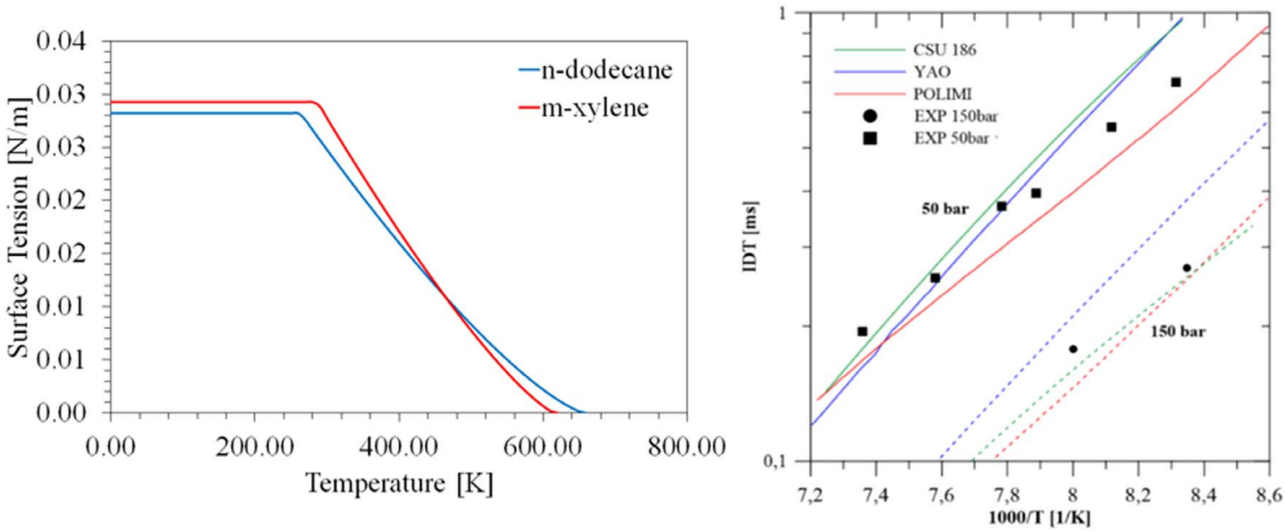

Fig. 1 Surface tension behavior with temperature for n-dodecane and m-xylene (left) and (*b*) ignition delay times comparison between experimental and numerical data obtained by CSU 186 [31], POLIMI [32], and YAO [33] mechanisms (right)

Table 2 Summary of the main global performance parameters for the three simulated cases

	OP1		OP2		OP3	
Engine parameter	Exp	Simulated	Exp	Simulated	Exp	Simulated
PES (%)	84.72%	84.70%	75.43%	75.57%	75.05%	75.45%
Intake mass (methane + air) (g)	2.672	2.668	2.712	2.692	2.705	2.673
η_{comb} (%)	84.33%	84.72%	82.99%	79.00%	91.74%	90.62%
IMEP (bar)	6.93	6.87	6.95	6.91	6.97	6.73

Note: IMEP: indicated mean effective pressure.

per injection. In this case, 85% of diesel fuel is injected during the first injection, while only 15% is injected during the second one.

The robustness of the model by varying rail pressure is then highlighted. Numerical results still exhibit good agreement with the experimental data even when the rail pressure is more than doubled.

Numerical results show good agreement also in terms of apparent heat release rate (AHRR) and cylinder pressure profiles (compared with Fig. 2) for all the simulated cases. In particular, both the LTHR and the high-temperature heat release (HTHR) timing and duration are well represented by the model for the single-injection case (Fig. 2, left). For reference, the maximum and minimum experimental AHRR and cylinder pressure profiles (after accounting for experimental uncertainties [35]) out of 1000 successive engine cycles as well as the corresponding ensemble-averaged profiles are shown with dash-dot and solid black lines, respectively.

Small discrepancies can be noted in terms of absolute values; however, the numerical results fit well within the experimental confidential intervals. Figure 2 (center) shows the results for the double injection at 500 bar. As for OP1, the LTHR timing and trend are well captured although the peak values are still overpredicted.

Conversely, the main combustion phasing trends and the peak HTHR values are predicted very well. The discrepancy in the AHRR curves during the expansion stroke may be due to underestimation of the heat transfer losses for the numerical case. The discrepancies between AHRR curves starting at 375 CAD are due to the underestimation of the ignition delay time for the combustion occurring after the second injection; in fact, in the numerical model, combustion is triggered almost instantaneously after the second injection, while there is a perceptible ignition delay time in the experiments.

Figure 2 (center) shows a good agreement for the pressure traces with a slight over prediction of the peak value. This is due to a slight overestimation of the predicted AHRR before top dead center.

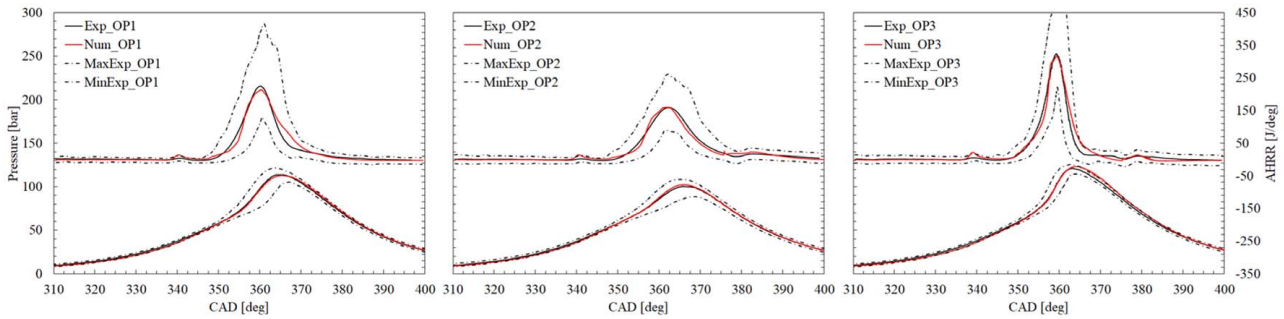

Fig. 2 AHRR (top) and pressure (bottom) profiles for OP1 (left), OP2 (center), and OP3 (right)

However, the predicted pressure lies within the maximum/minimum range over 1000 experimental cycles. AHRR and cylinder pressure profiles for the OP3 case are shown in Fig. 2 (right). The LTHR timing is predicted reasonably well, but peak LTHR is still slightly overestimated. The simulation ability to predict the main heat release (i.e., HTHR) during the combustion process is rather good in terms of timing and magnitude. The predicted AHRR is again within the maximum—minimum experimental AHRR range. The small discrepancies between the two curves do not affect substantially the prediction of the pressure trace and of the combustion efficiency. Predicted peak pressures are slightly higher than measured values during the first phase of the expansion stroke.

Fuels and Carbon Monoxide Mass Evolution

In Fig. 3, the in-cylinder mass evolution of methane, diesel, and CO over the cycle are presented along with the predicted AHRR curve superimposed for all the cases. For each operating condition, the LTHR is due to diesel low-temperature reactions, while methane combustion drives the HTHR.

In the OP1 case, the CO curve shows a peak during the first phase of methane combustion, being partially oxidized later in the combustion event (Fig. 3, left). This is due to methane oxidation reactions having a high reaction rate during the first phase leading to CO production followed by a slower conversion of CO to carbon dioxide (CO_2). Figure 3 (center) shows the results for OP2. The second diesel fuel injection starting at 375 CAD is not evident in the diesel curve as the combustion itself starts during the injection and the fuel burns almost instantaneously as testified by the CO increase.

The capability of the second injection to complete the oxidation of the bulk methane and the intermediate combustion products is evident by observing the methane curve inflection point after 380 CAD. The mass corresponding to the second CO peak, induced by diesel consumption, is entirely used toward the end of the combustion process, leading to a final CO value that is close to the one obtained after the main AHRR. This behavior underlines that the postinjection occurs when the bulk combustion is already terminated and that later injected diesel fuel would undergo complete oxidation mainly due to its high reactivity.

Results for OP3 are reported in Fig. 3 (right). The relatively high amount of diesel for the main injection coupled with a higher penetration and a more efficient stratification assures a faster methane combustion process. The small amount of unburned methane is oxidized completely along with CO at the end of combustion thanks to the second diesel injection.

Diesel Fuel Injection Analysis

A more detailed analysis of the 3D fields of flow and species is provided in the following sections for both injection and combustion processes. All the images refer to a top view of the engine according to the sketch shown in Fig. 4.

In Fig. 4 (left), the diesel vapor phase is represented as a contour of the 1% mass fraction value during injection at 500 bar.

These images show how in-cylinder turbulence and charge motion affect the mixing process. In the area under the intake valves, the jets are pushed close to the liner and the cylinder head, while on the other side, the air motion confines the jet in the central region of the chamber. This behavior leans out the diesel–air mixture close to the intake valves and enriches it close to the exhaust valves. The lack of symmetry of sprays induced by the organized charge motion is also evident.

The results for the 1200 bar injection case are shown in Fig. 4 (right) to evaluate the effects of the injection pressure on the

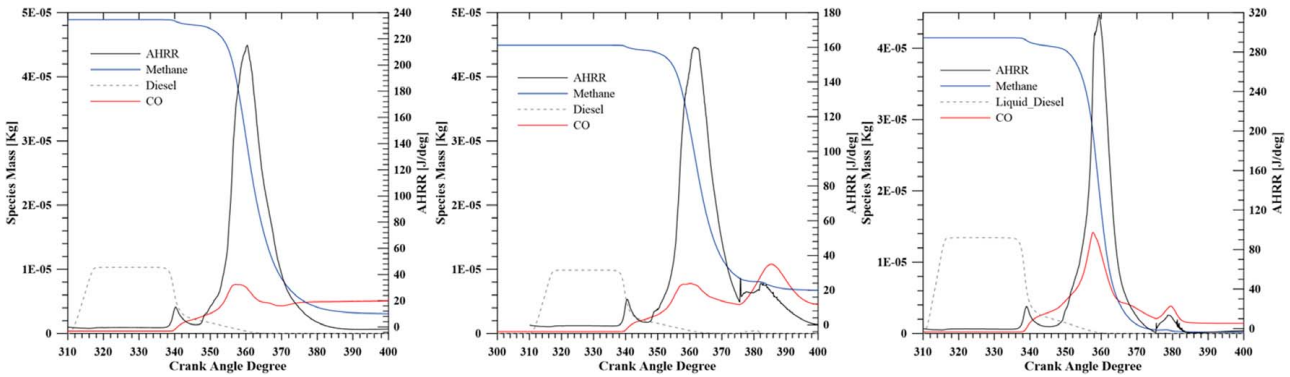

Fig. 3 Species mass evolution for OP1 (left), OP2 (center), and OP3 (right)

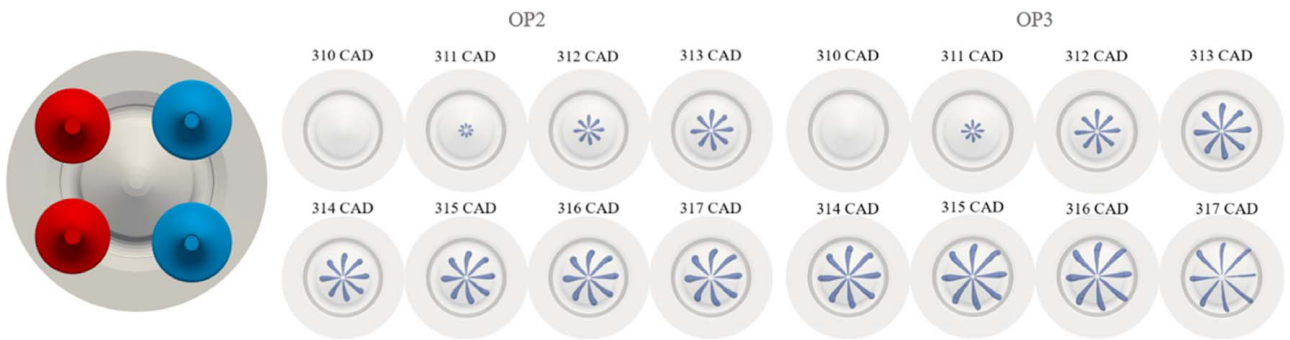

Fig. 4 The top view of the cylinder used for the 3D visualization, reporting the exhaust (left side) and intake (right side) valves and diesel fuel vapor phase as a contour of the 1% mass fraction value for OP2 (left) and OP3 (right)

spray penetration and diesel fuel distribution. The higher rail pressure allows for a greater diesel vapor penetration and better distribution. In this case, the spray overcomes the piston bowl projection, with no impingement on the liner or on the piston head. Furthermore, the higher fluid velocity during the injection process gives a greater spray momentum that is less affected by charge motion and is more symmetrical on both the intake and exhaust sides of the combustion chamber.

Ignition and Combustion Processes

The different in-cylinder diesel distributions at different injection pressures have been highlighted so far. In this section, supported by the role of diesel fuel, a two-dimensional (2D) cross section obtained from the three-dimensional (3D) distributions of the subsequent ignition and combustion processes is highlighted. Diesel and methane species and the product between formaldehyde (CH_2O) and OH species concentrations [36] are used to analyze the combustion process. The last two species are useful to track the oxidation evolution as they are highly reactive species produced during the low-temperature combustion and high-temperature combustion subprocesses, highlighting the oxidizing regions.

Figure 5 (left) shows the trend of T_{mean} and T_{max} as functions of CAD along with the AHRR curve. From the numerical point of view, the two temperature profiles assume specific meanings: the first is the maximum value reached among all computational cells inside the domain at a given CAD and the second represents the mean value. The start of the main stage of AHRR is coupled with a sharp increase in the maximum temperature inside the domain.

Moreover, since T_{mean} is not as significantly affected by the start of combustion, this implies that the highest temperature occurring during the ignition of the mixture is presented by a small number of cells. The following figures give a better understanding of the ignition and combustion phenomena.

Figure 6 (left) shows the diesel fuel distribution and its subsequent consumption for the single-injection case at 500 bar calculated on a 2D cross section at 10 mm below the cylinder head fire deck. It is evident from the images shown between 338 CAD and 348 CAD that the advanced injection timing gives sufficient time for turbulent mixing to distribute the diesel fuel throughout the combustion chamber. At 350 CAD, it can be seen that the main AHRR start occurs right after diesel ignition in two different spots where the equivalence ratio and the thermodynamic conditions are favorable. A few degrees later, the combustion process also begins in other regions closer to the wall where the diesel fuel concentration is lower but temperature is higher. At 366 CAD, diesel combustion is completed.

Figure 6 (center) shows how the methane consumption starts where diesel fuel is ignited; in the last frame, it can be seen that the combustion front is not able to propagate close to the liner, leading to a rather high fraction of unburned methane at the end of expansion. This behavior is typical for a very lean premixed

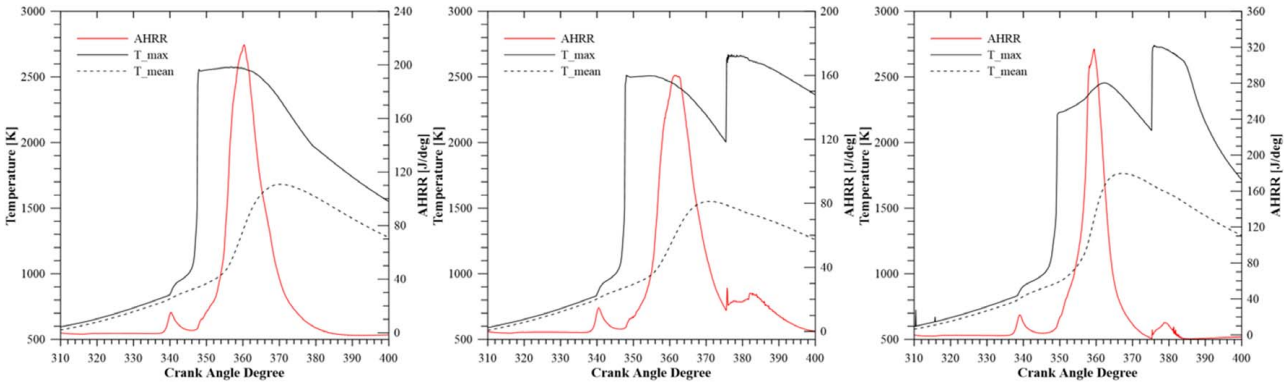

Fig. 5 Numerical temperature trends and predicted AHRR for OP1, OP2, and OP3

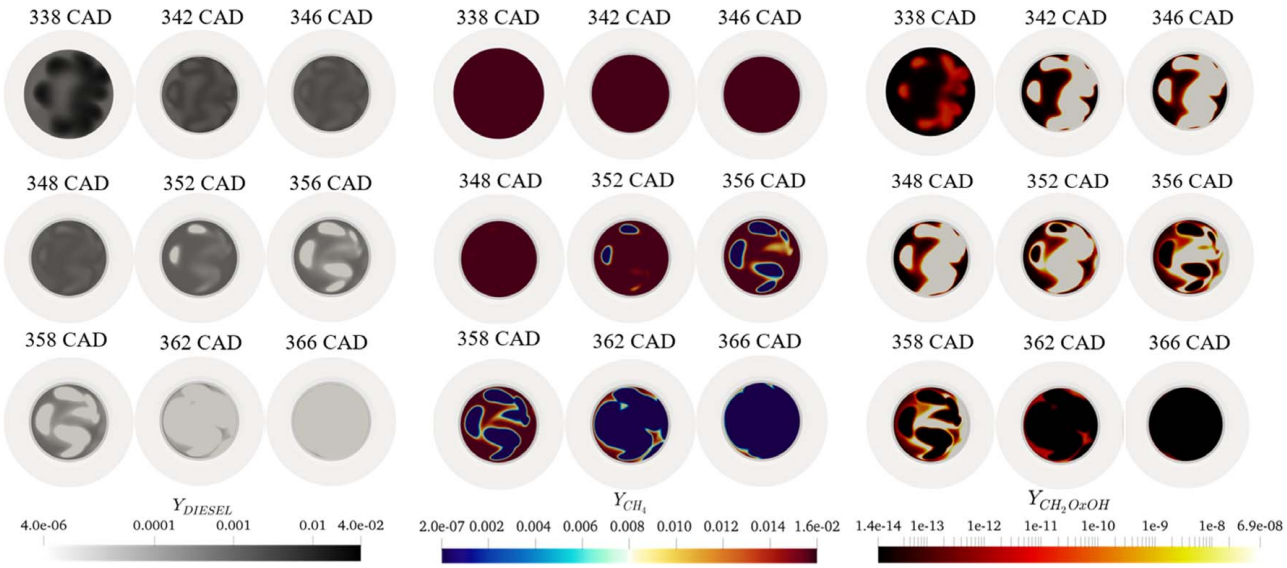

Fig. 6 Evolution of diesel fuel consumption (left), methane consumption (center), and $CH_2O \times OH$ production (right) during combustion for OP1

combustion process as the combustion propagation cannot be supported thermally in all the regions within the combustion chamber, and the heat transfer through the walls and the piston expansion cool down the mixture close to the liner, quenching the oxidation process. Figure 6 (right) presents the product of CH_2O and OH, indicating the regions where the combustion propagation occurs.

It can be seen that the "cold reactions" are distributed in all the regions and even more so whenever the diesel fuel is mixed more effectively. However, the combustion starts in two locations at the tip of the jets near the exhaust side where the diesel fuel concentration is greater and temperature is higher thanks to the piston wall influence.

Another observation can be drawn about the last part of the combustion process: the oxidation quenching occurring close to the liner wall at 364 CAD and the subsequent rapid cooling are the main reasons for the rather high CO levels at EVO. The need for keeping UHC and CO emissions low is in fact the main driver for the introduction of multiple injections to try and enhance the effectiveness of the oxidation process toward the end of the combustion process. The second injection produces an instantaneous increase of T_{max}. However, since the mean temperature is almost unchanged (Fig. 5—center), it is evident that this temperature increase is restricted only to rather small, localized regions of the combustion chamber, and therefore, the temperature increase is not able to fully support oxidation reactions throughout the chamber. The 2D images for fuel consumption and combustion propagation are shown later in this study.

Figure 7 (left) shows diesel fuel distribution and consumption calculated over a 2D section 10 mm below the fire deck. It is evident that diesel consumption starts at 352 CAD on the exhaust side of the chamber, where the mixture is richer, and then some CAD later, ignition occurs in the leaner region. It must be emphasized that, in both cases, combustion starts at the tip of the diesel jet close to the hot walls. The injected amount of diesel fuel is consumed completely during the first phase of the main AHRR to trigger methane combustion. The second injection occurring at 375 CAD is evident only few degrees later as the surface is located at 10 mm below the fire deck and only a small amount of diesel is able to reach it due to rapid evaporation and combustion.

Figure 7 (center) shows the methane consumption during the combustion process for the double-injection case at 500 bar (OP2). The methane consumption starts after the first diesel ignition in the exhaust side of the chamber where the equivalence ratio is higher, followed by the ignition of the leaner intake side. After ignition, it is evident that the combustion process gets faster in the chamber core and then proceeds slower toward the walls.

The second injection takes place when the combustion front approaches the liner wall, and then, there is still a significant fraction of unburned methane left elsewhere in the combustion chamber. It must be noted that the bulk of the unburned methane layer is in the exhaust region of the cylinder, where the first ignition occurs due to the greater distance of the diesel from the liner. On the other side, where the charge motion pushes the diesel toward the

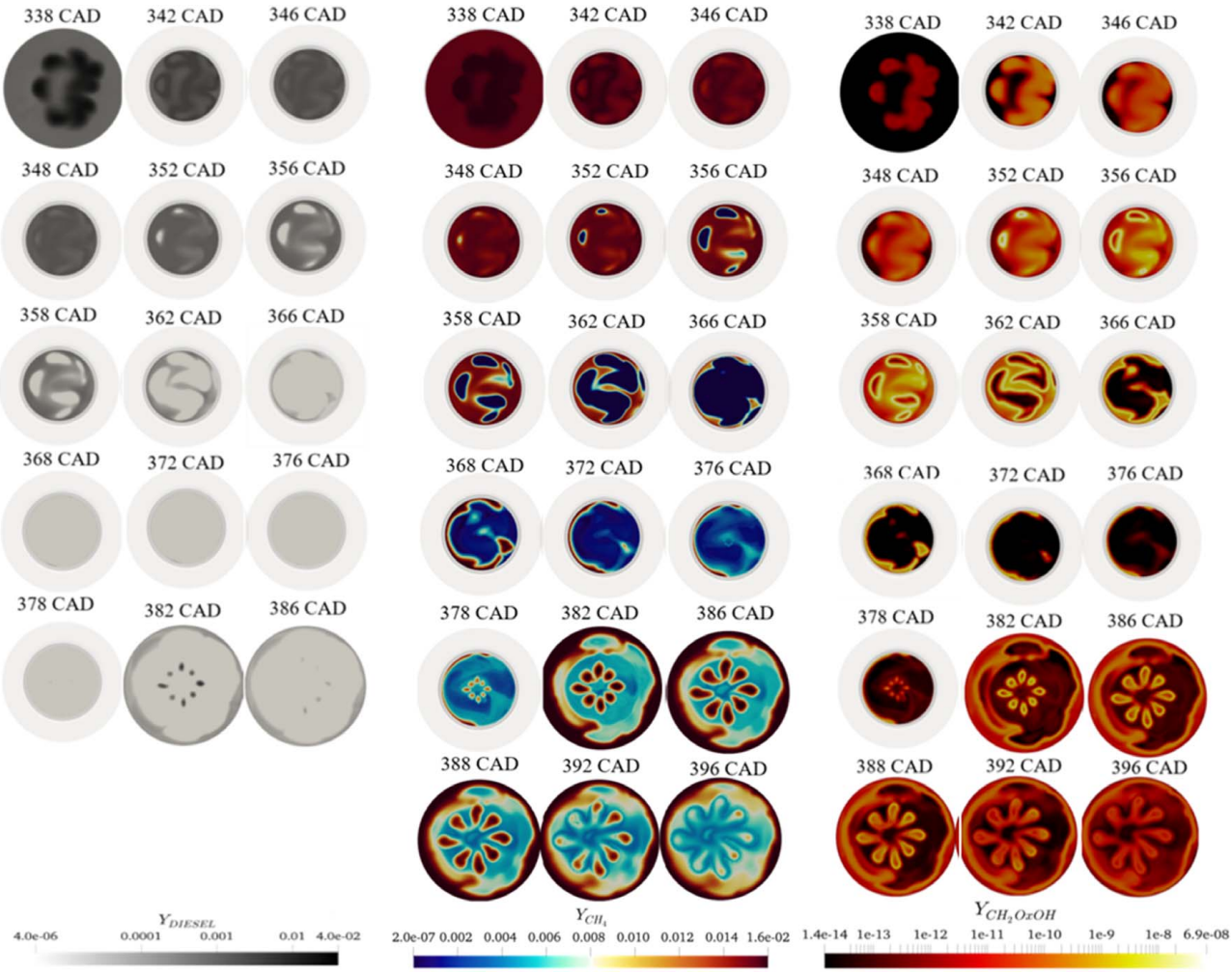

Fig. 7 Evolution of diesel fuel consumption (left), methane consumption (center), and $CH_2O \times OH$ production (right) during combustion for OP2

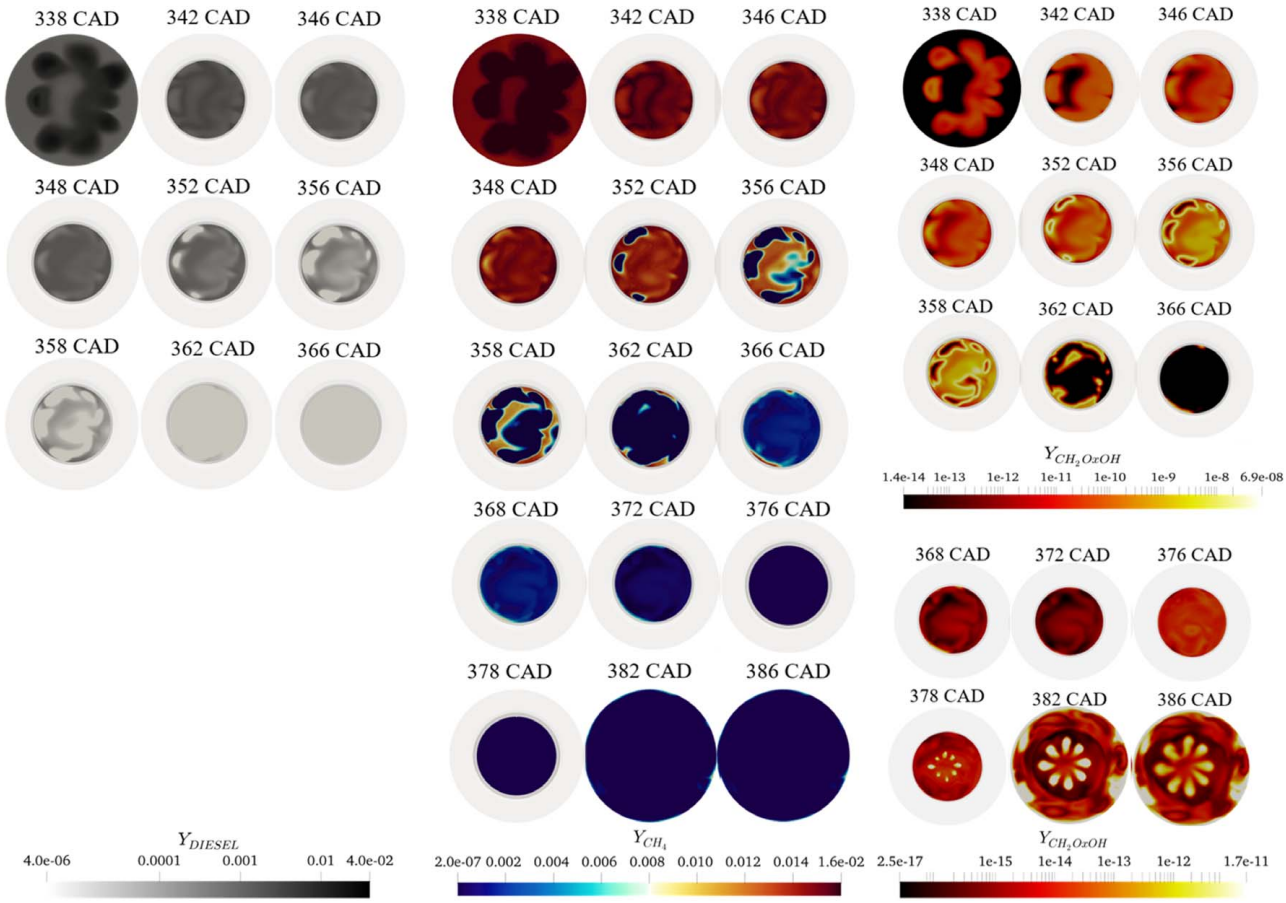

Fig. 8 Evolution of diesel fuel consumption (left), methane consumption (center), and $CH_2O \times OH$ production (right) during combustion for OP3

wall, the ignition is delayed but the enhanced mixing promotes a more effective combustion process, allowing oxidation close to the cylinder periphery. The postinjected diesel amount supports methane consumption only in the volume where the spray is able to penetrate (Fig. 7 (center)—CAD 378-396), but on the other hand, the combustion front generated is not able to propagate toward the liner to oxidize fully the methane fraction left.

Figure 7 (right) shows the combustion front propagation. The product between CH_2O and OH species can be used to emphasize also the LTHR start at 340 CAD. During the first phase of the combustion process, the methane is not involved yet, and the LTHR peak is only due to the initial diesel oxidation reactions.

The increased rail pressure does not affect the maximum temperature reached during combustion (Fig. 5—right); this explains why the NO_x emissions can be kept low. The second injection does not affect the mean temperature in the combustion chamber, but its effects are localized in a small region that is influenced by the diesel spray distribution.

Diesel and methane consumptions are reported with the 2D images for the double-injection case at 1200 bar (OP3) in Fig. 8 (left), where better diesel distribution can be observed compared with OP2, thanks to the higher rail pressure. Furthermore, combustion starts in more locations for OP3 compared to OP2, leading to a much faster diesel fuel combustion process.

The high rail pressure gives also richer diesel–air mixtures close to the wall; this is a key factor in reducing the unburned methane emissions as the combustion can get started far from the injectors (i.e., close to the wall), supporting a more complete methane oxidation. Diesel distribution after the post-injection is not presented here since the rather small amount injected and the high temperature give instantaneous evaporation and combustion.

Figure 8 (center) shows the methane consumption, highlighting the homogeneous and fast combustion process. The methane combustion starts close to the wall near the locations where diesel ignition first occurs before igniting the surrounding methane–air mixture.

For OP3, methane consumption and combustion front propagation (Fig. 8, center and right) are very different from OP2 as the combustion starts far from the walls, giving an almost complete gaseous fuel oxidation close to the wall during the first combustion phase. It is evident that the key difference between OP3 and OP2 lies in the opposite direction of the combustion front propagation (i.e., from the wall to the core) for OP3, which is important to avoid the production of the unburned fuel layer due to oxidation quenching. When post-injection occurs, the combustion is already almost over, thus promoting the oxidation of rather small amounts of methane located close to the spray zone; the combustion front cannot be propagated due to very lean conditions and the rather low charge temperature.

Table 3 presents the combustion phasing and duration for each case tested to further emphasize the differences between the three operating conditions.

Table 3 Combustion phasing and duration for each case tested

Operating condition	CA10	CA50	CA90	Combustion duration
OP1	354.3	364.2	377.2	22.9
OP2	352.1	360.5	364.3	12.2
OP3	340.0	354.2	356.4	16.4

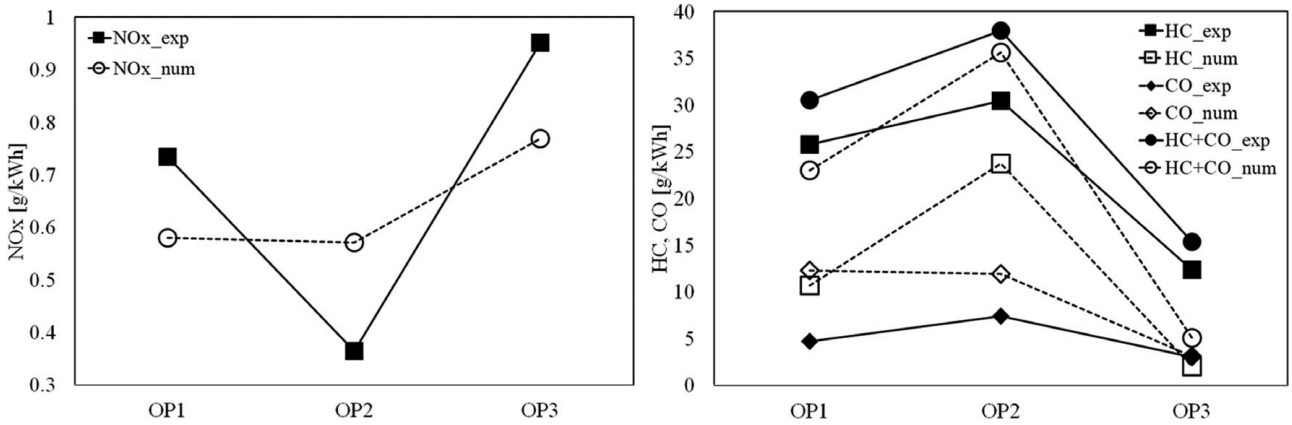

Fig. 9 Trend of NO_x emissions (left) and UHC, CO, and UHC + CO emissions (right)

Analysis of Emissions

In Fig. 9 (left), the predicted NO_x emission trends are presented and compared with experimental NO_x trends for all three operating conditions. Starting from the single injection at 500 bar (OP1) to the double injection at 1200 bar (OP3), the increasing trend in NO_x emissions is predicted well although the magnitudes are different from the corresponding experimental values. On the other hand, the NO_x reduction between the single 500 bar and the double 500 bar injection is not predicted very accurately, although a slight decrease can be highlighted. It must be stressed that these NO_x values are hard to capture as they are always below 1 g/kWh.

In Fig. 9 (right), the CO, UHC, and CO + UHC emission trends are reported; it must be highlighted that the CO absolute value is predicted rather accurately only for the 1200 bar double-injection case, while in all the other cases it is overestimated. The CO reduction moving from the single-injection case at 500 bar to the 1200 bar double-injection case is estimated rather well, as well as the increase in CO emissions for the double injection at 500 bar. This figure shows also the positive effects due to the adoption of the double injection at 1200 bar on CO reduction; in this case, an oxidation catalyst is required to meet current emission standards.

For what concerns the UHC emission, the model is rather accurate in predicting the increase moving from the single-injection case to the double-injection case at 500 bar as well as the decrease with the adoption of the double injection at 1200 bar. However, the absolute numerical values are underestimated systematically. The overall predictions of the CO + UHC trends appear good although the predicted magnitudes are still lower, showing that the combustion efficiency is overestimated in the numerical calculations.

Conclusions

Results from CFD simulations of a single-cylinder heavy-duty engine operating on dual-fuel diesel–methane low-temperature combustion at 5 bar BMEP and 85% and 75% percentage energy substitution (PES) by methane and with single- and double-diesel injections are presented in this article. The 3D CFD model developed has been validated first for the single-injection case at 500 bar and then for multiple injections and different rail pressures. The numerical analysis has shown different combustion behaviors explaining the different performance and production of pollutant emissions for each case.

In particular, it has been shown how, at higher rail pressures, diesel fuel is pushed out of the central zone of the combustion chamber, ensuring that the combustion starts closer to the cylinder wall and the methane present in near-wall regions is burned before quenching occurs due to heat losses. This phenomenon is enhanced also because the first phase of combustion and methane consumption occurs when the piston is still reversing the stroke and the volume increase does not yet lead to the rapid cooling of the mixture.

Moreover, the results obtained with the CFD simulations allow drawing the following further conclusions:

- The early SOI of 310 CAD provides sufficient time for diesel spray penetration and turbulent mixing to yield a rather distributed combustion process.
- The higher amount of CO and UHC obtained for the 500 bar rail pressure cases compared to the 1200 bar case was shown to be a consequence of differences in the ignition locations and the number of ignition spots (which were greater for the higher rail pressure).
- The greater number of ignition locations observed for the 1200 bar case explains the higher peak AHRR observed at higher rail pressures. In fact, this is driven by the rapid growth and coalescence of the combustion front from the ignition spots, resulting in faster methane reaction rates compared with the 500 bar cases.
- Higher UHC and CO emissions for the double-injection case at 500 bar pressure indicate poor combustion quality occurring after the postinjection. The increase in partial oxidation products can be attributed to the slower evolution of the main combustion process induced by the lower amount of diesel injected with the first injection. Moreover, the second injection is not able to generate a stable combustion front and a sufficiently high mean temperature rise as the combustion is confined within the regions reached by the diesel sprays.
- Due to the interaction between the in-cylinder charge motion, the spray injection does not exhibit symmetric properties, eventually leading to different combustion behaviors at different engine operating conditions.

Acknowledgment

The authors acknowledge the contribution of Mr. Lorenzo Berchicci in running the simulations for the dual injection cases presented in this article. The CINECA award under the ISCRA initiative is acknowledged, for the availability of high performance computing resources and support. S. R. K. and K. K. S. gratefully acknowledge funding for this work from the Alliance for Sustainable Energy, LLC, Managing and Operating Contractor for the National Renewable Energy Laboratory for the U.S. Department of Energy.

Conflict of Interest

There are no conflicts of interest.

References

[1] U.S. Department of Energy, 2009, "Basic Research Needs for Clean and Efficient Combustion of 21st Century Transportation Fuels—Report of the Basic Energy Sciences Workshop," https://science.osti.gov/

[2] EIA, 2018, "Annual Energy Outlook," https://www.eia.gov/outlooks/aeo/av.php, Accessed March 16, 2019.

[3] U.S. EPA 40 CFR Parts 9, 22, 85 et al.; NHTSA 49 CFR Parts 523, 534 et al., "Greenhouse Gas Emissions and Fuel Efficiency Standards for Medium and Heavy-Duty Engines and Vehicles -Phase 2; Final Rule," Federal Register, 2016.

[4] State of California Air Resources Board, 2013, "Evaluating Technologies and Methods to Lower Nitrogen Oxide Emissions From Heavy-Duty Vehicles, Resolution 13-27," http://www.arb.ca.gov/board/books/2013/062713/prores1327.pdf

[5] US Department of Energy, 2016, "Energy Department Announces $137 Million Investment in Commercial and Passenger Vehicle Efficiency," https://www.energy.gov/articles/energy-department-announces-137-million-investment-commercial-and-passenger-vehicle

[6] Reitz, R. D., and Duraisamy, G., 2015, "Review of High Efficiency and Clean Reactivity Controlled Compression Ignition (RCCI) Combustion in Internal Combustion Engines," Prog. Energy Combust. Sci., **46**, pp. 12–71.

[7] Redtenbacher, C., Kiesling, C., Malin, M., Wimmer, A., Pastor, J. V., and Pinotti, M., 2018, "Mattia Pinotti Potential and Limitations of Dual Fuel Operation of High Speed Large Engines," ASME J. Energy Resour. Technol., **140**(3), p. 032205.

[8] Nithyanandan, K., Zhang, J., Li, Y., Meng, X., Donahue, R., Lee, C.-F., and Dou, H., 2016, "Huili Dou Diesel-Like Efficiency Using Compressed Natural Gas/Diesel Dual-Fuel Combustion," ASME J. Energy Resour. Technol., **138**(5), p. 052201.

[9] Mitchell, R. H., and Olsen, D. B., 2018, "Extending Substitution Limits of a Diesel–Natural Gas Dual Fuel Engine," ASME J. Energy Resour. Technol., **140**(5), p. 052202.

[10] Polk, A. C., Gibson, C. M., Shoemaker, N. T., Srinivasan, K. K., and Krishnan, S. R., 2013, "Analysis of Ignition Behavior in a Turbocharged Direct Injection Dual Fuel Engine Using Propane and Methane as Primary Fuels," ASME J. Energy Resour. Technol., **135**(3), p. 032202.

[11] Srinivasan, K. K., Krishnan, S. R., Jha, P. R. and Mahabadipour, H., 2019, "Cyclic Variations in Diesel-NG Dual Fuel Engines," *Natural Gas Engines for Transportation and Power Generation*, K. K. Srinivasan, A. K. Agarwal, S. R. Krishnan, and V. Mulone, eds., Springer Verlag, Berlin, Germany.

[12] Srinivasan, K. K., Krishnan, S. R., and Qi, Y., 2013, "Cyclic Combustion Variations in Dual Fuel Partially Premixed Pilot-Ignited Natural Gas Engines," ASME J. Energy Resour. Technol., **136**(1), p. 012003.

[13] Krishnan, S. R., Srinivasan, K. K., Singh, S., Midkiff, K. C., Bell, S. R., Gong, W., Fiveland, S. B., and Willi, M., 2004, "Strategies for Reduced NO_x Emissions in Pilot-Ignited Natural Gas Engines," ASME J. Eng. Gas Turbines Power, **126**(3), pp. 665–671.

[14] Singh, S., Krishnan, S. R., Srinivasan, K. K., Midkiff, K. C., and Bell, S. R., 2004, "Effect of Pilot Injection Timing, Pilot Quantity, and Intake Charge Conditions on Performance and NO_x Emissions for an Advanced Low-Pilot-Ignited Natural Gas Engine," Int. J. Engine Res., **5**(4), pp. 329–348.

[15] Srinivasan, K. K., Krishnan, S. R., Singh, S., Midkiff, K. C., Bell, S. R., Gong, W., Fiveland, S. B., and Willi, M., 2006, "The Advanced Low Pilot-Ignited Natural Gas Engine—A Combustion Analysis," ASME J. Eng. Gas Turbines Power, **128**(1), pp. 213–218.

[16] Raihan, M. S., Guerry, E. S., Dwivedi, U., Srinivasan, K. K., and Krishnan, S. R., 2014, "Experimental Analysis of Diesel-Ignited Methane Dual Fuel Low Temperature Combustion in a Single Cylinder Diesel Engine," J. Energy Eng, **141**(2).

[17] Guerry, E. S., Raihan, M. S., Srinivasan, K. K., Krishnan, S. R., and Sohail, A., 2016, "Injection Timing Effects on Partially Premixed Diesel–Methane Dual Fuel Low Temperature Combustion," Appl. Energy, **162**, pp. 99–113.

[18] Tomita, E., Kawahara, N., Piao, Z., and Yamaguchi, R., 2002, "Effects of EGR and Early Injection of Diesel Fuel on Combustion Characteristics and Exhaust Emissions in a Methane Dual Fuel Engine," SAE Technical Paper 2002-01-2723.

[19] Azimov, U., Tomita, E., Kawahara, N., and Harada, Y., 2011, "Premixed Mixture Ignition in the End-Gas Region (PREMIER) Combustion in a Natural Gas Dual-Fuel Engine: Operating Range and Exhaust Emissions," Int. J. Engine Res., **12**(5), pp. 484–497.

[20] Königsson, F., Kuyper, J., Stalhammar, P., and Angstrom, H., 2013, "The Influence of Crevices on Hydrocarbon Emissions From a Diesel-Methane Dual Fuel Engine," SAE Int. J. Engines, **6**(2), pp. 751–765.

[21] Sohail, A., 2015, "An Experimental Investigation of Dual-Injection Strategies on Diesel-Methane Dual-Fuel Low Temperature Combustion in a Single Cylinder Research Engine," M.S. thesis, Department of Mechanical Engineering, Mississippi State University, Starkville, MS.

[22] Raihan, M. S., 2014, "A Comparative Study of Diesel-Ignited Methane and Propane Dual Fuel Low Temperature Combustion in a Single Cylinder Research Engine," M.S. thesis, Department of Mechanical Engineering, Mississippi State University, Starkville, MS.

[23] Richards, K. J., Senecal, P. K., and Pomraning, E., 2015, *CONVERGE CFD Manual*, Convergent Science, Madison, WI.

[24] Aniello, A., Bartolucci, L., Cordiner, S., Mulone, V., Krishnan, S. R., and Srinivasan, K. K., 2018, "CFD Analysis of Diesel-Methane Dual Fuel Low Temperature Combustion at Low Load and High Methane Substitution," ASME 2018 Internal Combustion Engine Division Fall Technical Conference, San Diego, CA, November.

[25] Jha, P. R., Krishnan, S. R., and Srinivasan, K. K., 2017, "Influence of Swirl Ratio on Diesel-Methane Dual Fuel Combustion: A CFD Investigation," Proceedings of the ASME 2017 Internal Combustion Engine Fall Technical Conference (ICEF2017), Seattle, WA, Oct. 15–18, Paper No. ICEF2017-3683.

[26] Königsson, F., and Stalhammar, P., 2012, "Controlling the Injector Tip Temperature in a Diesel Dual Fuel Engine," SAE Technical Paper, Paper No. 2012-01-0826.

[27] Leuthel, R., Pfitzner, M., and Frobenius, M., 2008, "Numerical Study of Thermal-Fluid-Interaction in a Diesel Fuel Injector," SAE Technical Paper, Paper No. 2008-04-2760.

[28] Bartolucci, L., Carlucci, A. P., Cordiner, S., Ficarella, A., Laforgia, D., Mulone, V., Rocco, V., Strafella, L., and Strafella, L., 2018, "Dual-Fuel Injection Fundamentals: Experimental—Numerical Analysis Into a Constant-Volume Vessel," Energy Procedia, **148**, pp. 18–25.

[29] Som, S., Rodriguez, A. I., Longman, D. E., and Aggarwal, S. K., 2011, "Effect of Nozzle Orifice Geometry on Spray, Combustion and Emission Characteristics Under Diesel Engine Conditions," Fuel, **90**(3), pp. 1267–1276.

[30] Versteeg, H., and Malalasekra, W., 2009, *An Introduction to Computational Fluid Dynamics*, Pearson, London, UK.

[31] Hockett, A. J., Hampson, J., and Marchese, A. J., 2017, "Natural Gas/Diesel RCCI CFD Simulations Using Multi-Component Fuel Surrogates," Int. J. Powertrains, **6**(1), p. 76.

[32] Stagni, A., Frassoldati, A., Cuoci, A., Faravelli, T., and Ranzi, E., 2016, "Skeletal Mechanism Reduction Through Species-Targeted Sensitivity Analysis," Combust. Flame, **163**, pp. 382–393.

[33] Yao, T., Pei, Y., Zhong, B. J., Som, S., Lu, T., and Luo, K. H., 2017, "A Compact Skeletal Mechanism for n-Dodecane With Optimized Semi-Global Low-Temperature Chemistry for Diesel Engine Simulations," Fuel, **191**, pp. 339–349.

[34] Petersen, E., Davidson, D., and Hanson, R., 1999, "Kinetics Modeling of Shock-Induced Ignition in Low-Dilution CH4/O2 Mixtures at High Pressures and Intermediate Temperatures," Combust. Flame, **117**(1–2), pp. 272–290.

[35] Partridge, K. R., Jha, P. R., Mahabadipour, H., Krishnan, S. R., and Srinivasan, K. K., 2018, "Systematic Uncertainty Considerations in the Comparison of Experimental and Computed Cylinder Pressure and Heat Release Histories," Proceedings of the ASME 2018 Internal Combustion Engine Fall Technical Conference (ICEF2018), San Diego, CA, Nov. 4–7, Paper No. ICEF2018-9707.

[36] Li, Z. S., Li, B., Sun, Z. W., Bai, X. S., and Aldén, M., 2010, "Turbulence and Combustion Interaction: High Resolution Local Flame Front Structure Visualization Using Simultaneous Single-Shot PLIF Imaging of CH, OH, and CH2O in a Piloted Premixed Jet Flame," Combust. Flame, **157**(6).